CONTROL OF SHROUD LEAKAGE LOSS AND WINDAGE TORQUE IN A LOW-PRESSURE TURBINE STAGE

Loizos Christodoulou[1], Zhihui Li[2], Stephen Ambrose[1], and Richard Jefferson-Loveday[3]
Richard Jackson[4], Gary Lock[4], Carl Sangan[4], and James Scobie[4]

[1] Gas Turbine and Transmissions Research Centre (G2TRC), Faculty of Engineering, University of Nottingham, Nottingham, NG7 2TU, United Kingdom

[2] Department of Aeronautics, Imperial College London, London, SW7 2AZ, United Kingdom

[3] Department of Engineering, King's College London, London, WC2R 2LS, United Kingdom

[4] Department of Mechanical Engineering, University of Bath, Bath, BA2 7AY, United Kingdom

ABSTRACT

As new aeroengine architectures move to larger diameter fans and rotors, the associated increase in weight will need to be counterbalanced by lighter, more compact, and more efficient low-pressure turbines (LPT). Efficiency gains in LPTs can be achieved by reducing the losses associated with the shroud leakage flows. Flow control studies on the topic have traditionally focused on reducing the mixing loss, which constitutes a considerable proportion of the total loss. Nonetheless, increasing engine speeds are driving additional gains obtained by also targeting the reduction of windage losses. Developing a flow control solution with the dual objective of reducing over-tip cavity mixing and windage losses has not previously been attempted. This is a challenge due to conflicting flow control requirements and geometric constraints. Reducing windage loss generally requires increasing the swirl-ratio of the leakage flow, while reducing mixing loss requires reducing this ratio to match that of the main gas path. The current work proposes a novel flow control solution to successfully achieve this purpose through the emerging technology of additive manufacturing. The successful flow control concept was developed through numerical simulation, printed using an additive manufacturing process, and validated in a purpose-built rig. Experiments and computations were consistent with a cumulative reduction in cavity windage of 16%. The FCC is estimated to increase the mechanical efficiency of the turbine stage in isolation by 1%.

Keywords: Turbines, Cavities, Sealing, Windage, Mixing, Flow Control, CFD.

1. INTRODUCTION

Minimizing the losses within a low-pressure turbine (LPT) system is critical for the design of next-generation ultra-high bypass ratio aero-engines. These new engines will host larger diameter fans and operate at higher rotor speeds. It is expected that windage torque in the stator-well and over-tip cavities will be a significant source of loss, influenced by the ingestion of mainstream annulus air with a tangential velocity opposite to that of the rotor.

A low-pressure turbine features a series of cavities at high and low radius, which aim to prevent ingestion and leakage of mainstream annulus air. Figure 1 highlights the cross-section of the LPT in a three-spool aero-engine. The inset shows 1.5 stages of the LPT in more detail (rotor-stator-rotor). At low radius, a stator-well cavity is formed of two wheel-spaces, connected by an interstage labyrinth seal. At high radius, the rotor shroud and fin tips form an over-tip cavity with the casing.

A stator-well cavity is shown in detail in Fig.2a. This configuration has been a recent subject of research through the EU Clean Sky 2 Programme [1-3]. The salient flow paths include ingress into the upstream wheel-space of the cavity (A), leakage through small tangential blade gaps (B), cooling flow (C), interstage leakage (D) minimized by the labyrinth seal on the axial drive arm of the rotor, and egress to the mainstream annulus

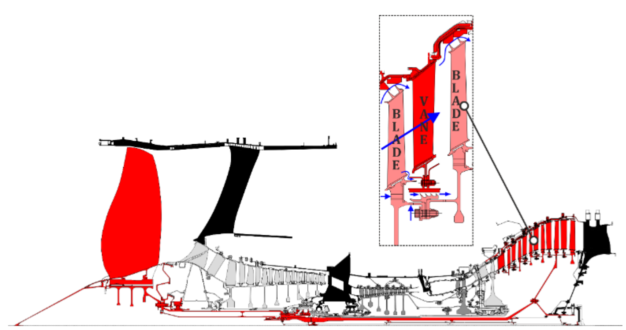

FIGURE 1: CROSS-SECTION OF A MODERN THREE-SPOOL AERO-ENGINE WITH THE LOW-PRESSURE SYSTEM IN RED.

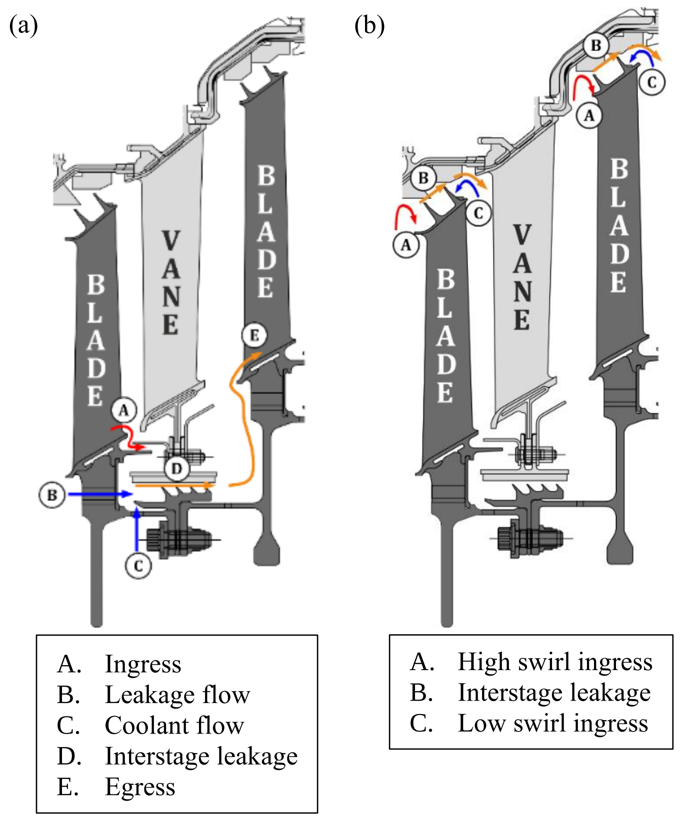

FIGURE 2: FLOW PATHS IN (a) A STATOR-WELL CAVITY, AND (b) AN OVER-TIP CAVITY.

(E). The flow paths in an over-tip cavity are shown in Fig.2b. Here the flow approaches the blade with a high swirl (positive). Some of this positively swirling flow is ingested into the upstream chamber of the over-tip cavity (labelled A). Since this has high, positive swirl, the relative windage contribution in the upstream chamber is small. A portion of this ingress will bypass the blade passage and instead traverse the fin tips (B), despite a small radial clearance achieved using an abradable lining (often honeycomb) on the casing. This interstage leakage will exit the downstream chamber as egress to the main annulus with a difference in swirl angle (the blade row has turned the flow from positive to negative swirl), causing an associated mixing loss. Some of the negative swirl will also be ingested into the downstream chamber (C), resulting in a windage loss due to the proximity of the negative swirl with the downstream rotor tip fin.

Experimental and numerical investigations of over-tip cavity flows reveal complex flow interactions between cavity and main flow, with the underlying mechanisms still a matter of debate [4-6]. Measurements from the exit cavity of a stationary blade row labyrinth system showed the existence of non-uniform flow with high circumferential velocity [4]. Highly-resolved flow data collected from the inlet cavity of a turbine rotor tip labyrinth seal revealed a toroidal vortex at the interface with the main flow [5]. Perini et al. [6] analyzed rotating instabilities formed inside an LPT over-tip cavity and identified unsteady flow structures uncorrelated with the blade-passing frequency. The complex flow interactions uncovered in these studies generate the so-called mixing losses [7, 8] but can also dominate the secondary flow inducing further losses downstream; the extent of influence depend on the clearances in the cavity among other parameters [9, 10]. The influence of radial gap and exit cavity size on yaw angle in the near-tip region of the main flow were also assessed through numerical simulation in an over-tip cavity model in a two-stage LPT [11]. Mixing loss is the creation of entropy due to viscous friction between the differing velocity streams of the main gas path and the re-entering leakage flow. This thermodynamically irreversible process causes a decrease of the stagnation pressure and an increase of the turbulence kinetic energy. In the current work, the mixing loss was visualized as a change in turbulence kinetic energy but quantified more precisely with the calculation of an isentropic efficiency for the turbine stage in isolation.

In terms of flow control concepts, Phau et al. [12] proposed design modifications such as non-axisymmetric profiling on the shroud based on the flow understanding gained from their experimental analysis of over-tip cavity flow structure. These were not evaluated rigorously but were predicted to offer a potential 0.2%-0.5% improvement in overall turbine efficiency. Later work investigated the use of turning vanes on the stator and rotor. A turbine rig was used to introduce a vane row in the downstream region of an over-tip cavity, which was shown to be effective in reducing loss by turning the leakage in the direction of the mainstream annulus flow [13]. The LPT efficiency increased by up to 0.4%, with the performance dependent upon the vane geometry and their spacing. Additional profile features were investigated in a separate study using the same experimental facility [14]. Results showed that chamfering and profiling the end wall and adding axial and radial deflectors all improved the stage efficiency. An optimized solution with a combination of these features generated an overall efficiency improvement of 0.75%. Wallis et al. [15] found that turning vanes on the rotor shroud reduced the tip leakage flow. Despite the intention to extract additional work from the vanes, the efficiency reduced owing to increased ingress into the downstream cavity, because of the reduced leakage. However, computational results show that turning vanes on the casing can improve the turbine efficiency if they are successful at turning the flow in the direction of the mainstream [16]. Passive tip-injection is a further flow control strategy that has been explored numerically by Ghaffari et al. [17] for a realistic LPT stage, where boundary conditions were taken from experiment without tip-injection. The principle of this approach was to apply aerodynamic resistance to the leakage flow to reduce its mass flow rate. Although their results did not show any reduction in the overall leakage mass flow rate, it was argued that the injected flow that made up a portion of the leakage contributed to the specific work of the stage. Further, there was also enhancement of the yaw angle at the cavity outlet.

Although there is evidence of LPT cavity flow control to reduce mixing losses and the downstream stage losses, there is no substantive research on the application of methods to reduce cavity windage torque. Minimizing windage torque is critical for

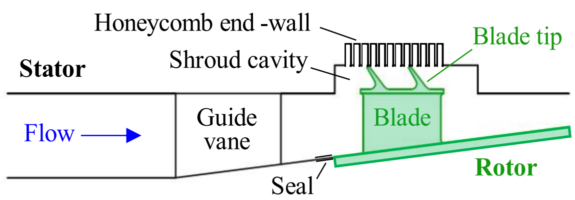

FIGURE 3: LOW-PRESSURE TURBINE STAGE

the development of next-generation ultra-high bypass ratio aero-engines. This paper presents a joint numerical and experimental campaign on the application of an optimized flow control concept (FCC) to reduce both the windage torque and the mixing losses in an LPT over-tip cavity. The FCC was a row of turning deflectors in the downstream chamber of the over-tip cavity, which redirected positively swirling flow onto the back face of the rotor fin to reduce the windage, whilst also turning the over-tip leakage in the direction of the main annulus flow to minimize mixing losses. It was optimized to perform most effectively with the honeycomb end-wall at an operating point representative of cruise flight conditions. The paper is structured as follows: details of the numerical model and experimental facility are in section 2, validation of the baseline flow, i.e., the flow without the FCC, is in section 3, development of the FCC through numerical simulation is in section 4, validation of the FCC is in section 5, and conclusions are in section 6.

2. METHODOLOGY

The engine-representative geometry and boundary conditions for the LPT stage were provided by the Clean Sky 2 topic manager. These were used to prepare numerical and experimental models at the Universities of Nottingham and Bath, respectively. A schematic of the LPT stage is shown in Fig.3. It consists of 32 stator vanes (inlet guide vanes) and 33 rotor blades in a converging annulus. The over-tip cavity is formed by the fins (forward-angled teeth) on the rotor shroud and the casing. The outer casing is at a constant radius, with an interchangeable honeycomb or solid end-wall.

2.1 Numerical model

The numerical model was prepared using the commercial software ANSYS, version 2020R2, and is shown in Fig.4(a). The domain consisted of multiple cell zones that exchange flow data during the simulation through mesh interfaces. There were four cell zones: the guide vane, the cavity, the blade, and the honeycomb. The cavity was interfaced with the guide vane and honeycomb using static interfaces, and with the rotating blade using sliding mesh interfaces. The blade tip and the rotor hub surfaces in the static cavity cell zone were defined as rotating no-slip walls. The inlet upstream of the guide vane was defined as a total pressure inlet. The outlet downstream of the blade was defined as a static pressure boundary, with prescribed pressure at the inner radius and a radial pressure distribution given by Eq.1, where p is static pressure, r is the radial coordinate, ρ is density, and V_t is the tangential velocity component. This radial pressure distribution eliminated backflow at the outlet. All other surfaces, not explicitly referred to here, were defined as static no-slip walls. The angular velocity of the rotating cell zone and wall surface zones, the total pressure at the inlet, and the inner pressure at the outlet were matched to the rig operating conditions.

$$\frac{\partial p}{\partial r} = \frac{\rho {V_t}^2}{r} \qquad (1)$$

Hexahedral meshes were generated for the cavity in ANSYS ICEM, and for the guide vane and blade blocks in ANSYS Turbogrid. The cavity mesh is shown in Fig.4(b). The guide-vane / blade meshes are shown in Fig.4(c); these and the rounded corners at the base of the teeth of the labyrinth seal teeth featured an o-grid topology. For the honeycomb, a tetrahedral mesh was generated in ANSYS Meshing. The mesh was refined in the near-wall regions, where large velocity gradients were expected, resulting in a y^+~1 at the walls. There was a negligible influence on the computations when the mesh density increased

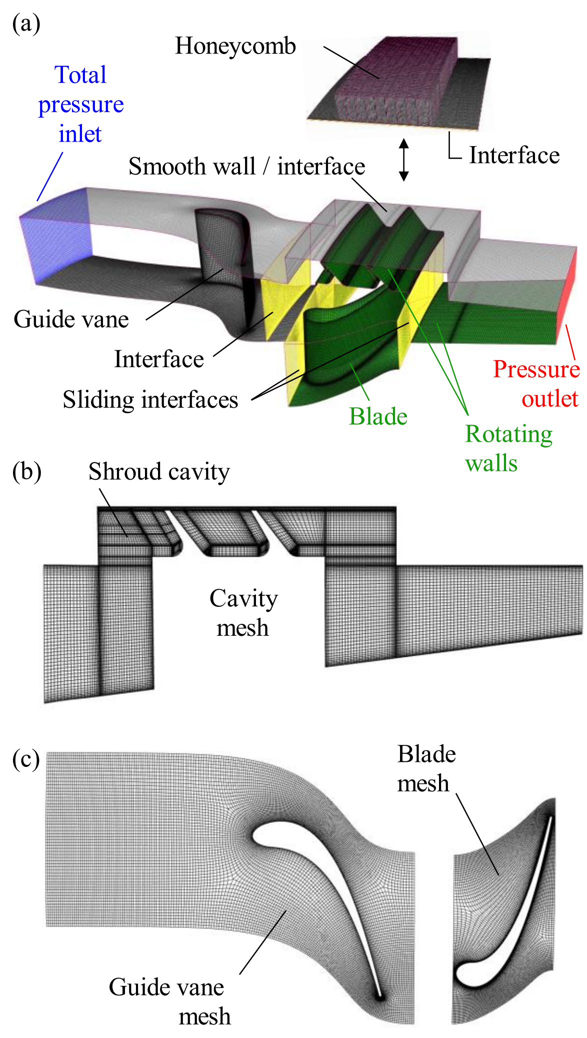

FIGURE 4: COMPUTATIONAL MODEL: (a) PERIODIC SECTOR WITH BOUNDARY TYPES, (b) CAVITY MESH, AND (c) GUIDE VANE AND BLADE MESHES

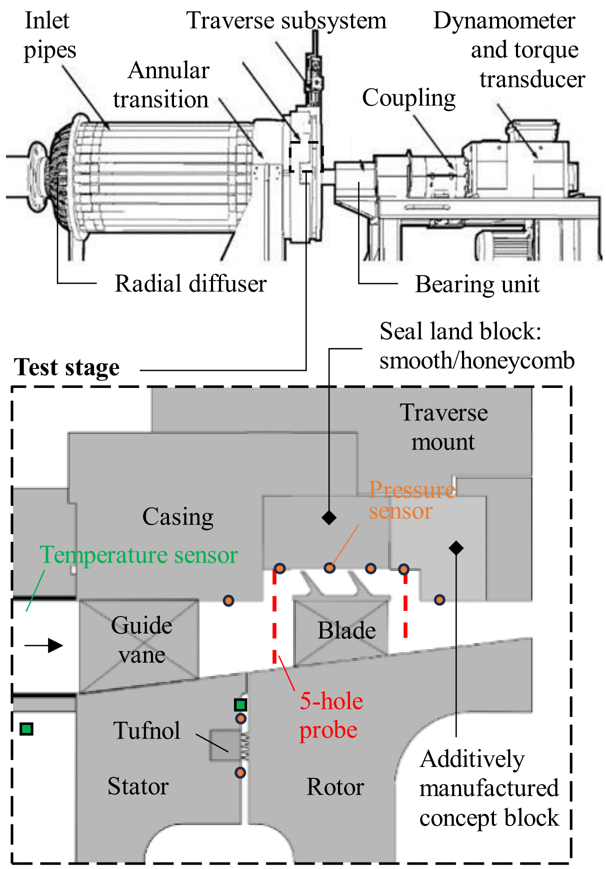

FIGURE 5: PURPOSE-BUILT LABORATORY RIG

by a factor of 1.5. Thus, the solution was considered mesh independent with a cell count of approximately 6.6 million cells.

The simulations were performed using the compressible URANS solver in ANSYS Fluent. A first order implicit scheme was used for the temporal discretization and second order schemes were used for the spatial discretization of the governing equations. Turbulence was modelled using the shear-stress transport k-ω model. For each time step of 10^{-5} s, inner iterations were performed until the maximum residual reached 10^{-6}. Mean quantities converged after a few shaft cycles. Simulations were performed with smooth and honeycomb end-walls for the baseline configuration, enabling a comparison between the numerically-predicted and experimental pressure distribution across the labyrinth seal. The honeycomb end-wall was used for the configuration with the FCC. The computational cost of a simulation was 1,600 and 4,000 core-hours per shaft cycle for the case with smooth and honeycomb end-walls, respectively.

The operating point of the cavity is defined by the pressure ratio across the cavity/blade, PR, and the swirl-ratio of the ingress into the upstream cavity, $X_{k,\,in}$. The full range of testing was in a design space 1.05 < PR < 1.22 and $0.55 < X_{k,\,in} < 1.05$. In the paper, we have presented detailed results at the design point, $X_{k,\,in} = 0.8$ and PR = 1.08. Results at other operating points were qualitatively similar and measurements of improved torque were achieved across the full range. The swirl-ratio is defined in Eq.2, where V_t is the tangential velocity component, Ω is the rotor angular velocity, and b is the shroud radius. In the current work, the cavity was operated at PR=1.08 and $X_{k,\,in}$=0.8. The rotational Reynolds number was $Re_\Phi = 1.6\text{x}10^6$.

$$X_k = \frac{V_t}{\Omega b} \qquad (2)$$

2.2 Experiment

The cold-flow axial turbine rig at the University of Bath was used to conduct experiments simulating the flow paths in an LPT over-tip cavity at fluid-dynamically scaled conditions, as shown in Fig.5. The test facility is described in Jackson *et al.* [2] but adapted from a stator-well to an over-tip cavity configuration.

The cross-section view of the test section is also shown in Fig.5, which includes the new outer band annulus, stator, and rotor. The annulus features a row of 32 stator vanes (inlet guide vanes) and a row of rotor blades. The over-tip cavity is formed by the fins on the rotor shroud and the casing. The rotor is manufactured from three parts, with the hub fixed to the shaft by a hydraulic coupling. The rotor featured 33 blades – the number of which was deliberately different to the number of inlet guide vanes, in order to minimize the risk of harmonic effects. Flow into and out of the rotor-stator wheel-space was minimized by a labyrinth seal. The seal teeth were machined into the upstream rotor face and radially aligned with abradable Tufnol on the stator surface opposite. The test rig operating conditions are listed in Table 1. The test facility was deliberately designed to simulate the over-tip cavity flow in isolation, assessing windage losses in an engine-representative environment at low TRL. This was a proof-of-concept study using additive manufacturing technology to extend the design envelope.

The in-line torque meter (HBM T12) described by Jackson *et al.* [2] was used to measure the change in windage between the baseline honeycomb end-wall and the FCC. The sensor was re-calibrated in-situ over the larger torque range expected to be measured during the experiments (0 to -50 Nm). To isolate the change in cavity windage from the other torque contributions (*e.g.*, bearing friction), a carefully controlled operating procedure was used for each test condition of $X_{k,\,in}$. As with the stator-well cavity experiments, the temperature of the bearing housing was closely monitored using a K-type thermocouple. A reference, steady-state temperature was found for the baseline

TABLE 1: TEST RIG OPERATING CONDITIONS

Parameter	Range	Design condition
N	0 → 6,000 rpm	4,000 rpm
$\dot{m}_A$	0 → 1.45 kg/s	~ 1.2 kg/s
Re_Φ	0 → $2.4\text{x}10^6$	$1.6\text{x}10^6$
$X_{k,\,in}$	0.55 → 1.05	0.8
PR	1.05 → 1.22	1.08

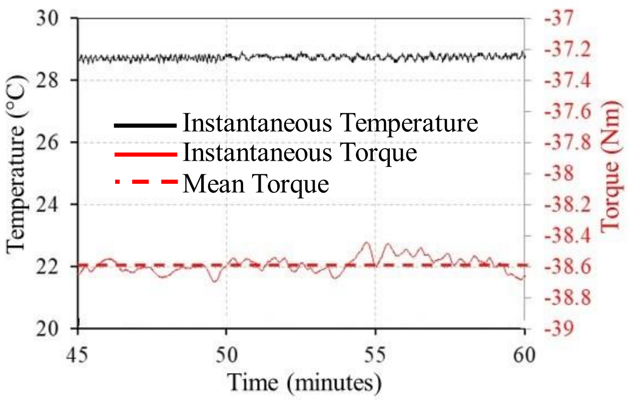

FIGURE 6: TORQUE AND BEARING TEMPERATURE TRACE

configuration over a small range of $X_{k,\,in}$. To ensure a fair torque comparison between the baseline and the FCC, the bearing temperature for the FCC experiments was closely matched to the reference baseline value (to within ±1 °C). Once this value was reached, the test data was collected. At each value of $X_{k,\,in}$, the torque data was sampled over 30 s at a rate of 80 Hz. To minimize noise, a 1 Hz low-pass filter was used, and a median average of the sample taken. The stability of the bearing temperature and the torque is shown in Fig 6. for an example case. The uncertainty in the torque measurement is +/- 0.02 Nm [2].

Although the cavity windage could not directly be measured, the change in windage was accurately determined. Since the other sources of torque were fixed using the preceding bearing warm-up method, the change in windage can be expressed non-dimensionally as a change in moment coefficient given by Eq. 3. Here, C_M is the rotor moment coefficient, M is the total measured torque, ρ is density, Ω is rotor angular velocity, and b is the shroud radius. Note that the sign convention is for M to be positive in the direction of rotation – therefore, negative values indicate a windage torque, and positive values indicate that power is generated (work done by the fluid on the rotor).

$$C_M = \frac{M}{{}^{1}\!/_{2}\,\rho \Omega^2 b^5} \qquad (3)$$

The remaining instrumentation for the pressure and swirl measurements are shown in Fig. 5. Static pressure taps were distributed in the main annulus across one vane pitch, upstream and downstream of the over-tip cavity. An axial distribution of pressure was also measured along the length of the over-tip cavity for the baseline and FCC configurations. The pressure drop across the rotor-stator labyrinth seal was monitored to ensure that the leakage remained minimal. The temperature near the labyrinth seal was measured to check that this did not exceed critical levels.

Gauge pressures were measured using four differential transducers (ESI PR3202) that were individually calibrated in-house. The transducers had a range of 0-400 mbar and an accuracy of ± 0.3% of the full-scale range (± 1.2 mbar). Each transducer was connected to a 48-channel Scani-valve system, allowing up to 192 pressure measurements to be made during a single experiment. The pressure data were acquired at 80 Hz and averaged over 2 s, following a settling period of a further 2 s.

The local velocity components and corresponding flow angles in the upstream and downstream chambers of the tip cavity were determined using pressure measurements from the same custom drilled-elbow five-hole probe as that used for the stator-well experiments. The radial coordinate of the probe was controlled using a bespoke traversing system. Five separate differential transducers (“All Sensors” 5PSI-D-PRIME-MV, 345 mbar range) simultaneously acquired the pressures, sampled at 1000 Hz over a 5 s period before being averaged. Flow angles and velocities were then derived by applying the data to calibration coefficients. These coefficients were provided by Vectoflow, following their in-house calibration of the probe.

The five-hole probe was also used to measure the mid-annulus swirl at the upstream traversing location (r/b = 0.96), when simultaneously collecting torque data. For these experiments, the probe pressure data was acquired at the same rate as the torque data (80 Hz) and averaged over the same sample period at each condition of X_k, in. This data was collected separately from that for the traversing experiments.

The flow control concepts were additively manufactured using stereolithography (SLA), printed by Laser Prototypes Europe Ltd with support on design for manufacture by Added Scientific Ltd. The synthetic printing material had a high stiffness to avoid deflection, with material properties that had similar characteristics to ABS/polypropylene. The FCCs were bonded together to form a ring, resulting in separate sub-assemblies, which could easily be interchanged in the rig.

3. BASELINE FLOW

Numerical and experimental results for the baseline configuration with smooth and honeycomb end-walls are shown in Fig.7. Note that the radial clearance between the teeth of the labyrinth seal and end-wall was identical for both cases. The contour plots in Fig.7 show the time-averaged and circumferentially-averaged swirl-ratio field from the numerical simulations. In-plane streamlines are superimposed on the contours to illustrate the predicted average flow structure in the axial-radial plane. The swirl-ratio field and flow structure are qualitatively similar for both end-walls. In the annulus, the swirl-ratio decreases from 0.8 to -0.4 as the flow passes through the blade row and generates power. The over-tip leakage flow enters the cavity near the upstream edge of the blade shroud, where it is subjected to the rotor pumping effect. It then passes between a recirculation zone on the stator side and a smaller recirculation zone on the rotor side before traversing the clearance of the labyrinth seal between the end-wall and a recirculation zone within the middle cavity. On exiting the seal, the leakage flow impinges on the radial wall of the downstream cavity and re-enters the main gas path. The leakage flow exits the downstream cavity on the stator side as egress. Low swirl-ratio fluid exiting the blade row is pumped up into the downstream cavity region between the rotor and leakage flow on the stator side as ingress.

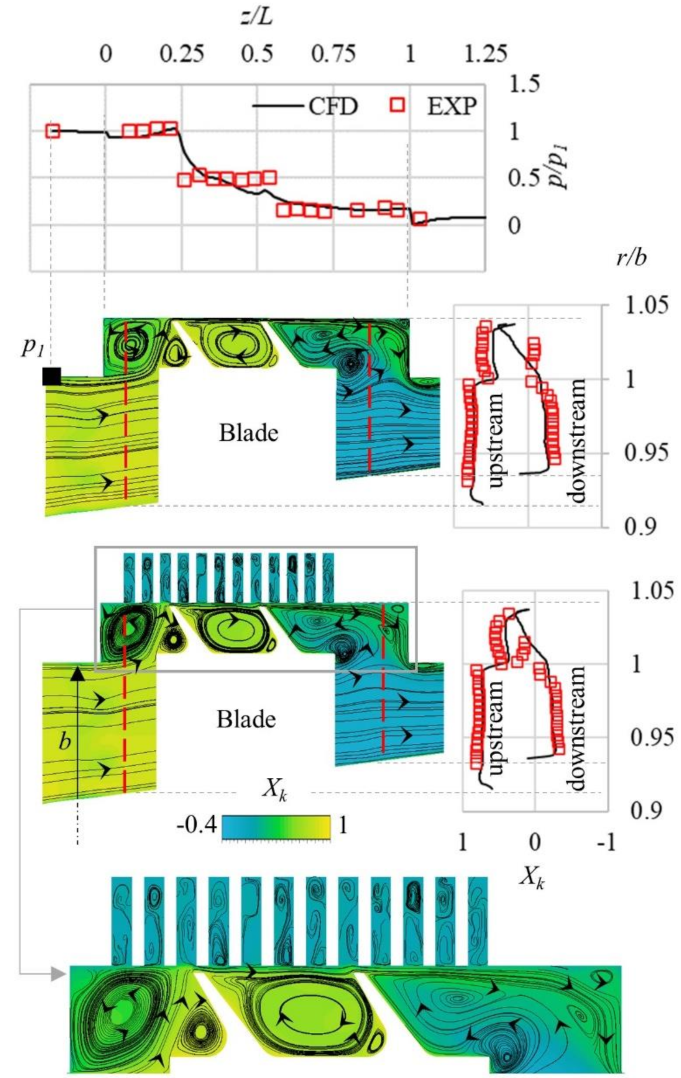

FIGURE 7: PRESSURE AND SWIRL IN THE BASELINE SHROUD CAVITY FOR SMOOTH AND HONEYCOMB END-WALLS (PR = 1.08 and $X_{k,\,in}$ = 0.8)

In the case of the honeycomb end-wall, the leakage flow fills the honeycomb cells with slow moving fluid that effectively produces a momentum deficit for the leakage flow. This is evident in the downstream cavity where there is an increased angle of incidence between the leakage streamlines of the leakage flow and the smooth section of end-wall downstream of the honeycomb.

The radial distributions of swirl-ratio in Fig.7 are taken at the two axial positions indicated by the vertical dashed lines on the contour plots. These datum lines traverse the upstream and downstream cavity/annulus. The numerical and experimental distributions of swirl-ratio are qualitatively consistent. There are quantitative discrepancies between simulation and experiment inside the cavity, most notably in the downstream cavity of the smooth end-wall. In general, the experimentally measured swirl-ratio in the cavity is always of larger magnitude than the numerical prediction. This is believed to be due to the presence of an opening on the shroud in the case of the experiment that was necessary for the probe traverse to move in and out of the test section.

The pressure distribution across the labyrinth seal in Fig.7 is for the smooth end-wall and shows good agreement between simulation and experiment. Specifically, this confirms that the mass flow rate of the numerically predicted leakage is accurate as it will be proportional to the pressure drop across the seal. The uncertainty in the pressure readings outlined in Section 2 was used to determine the measurement uncertainty for p/p_1, as shown in the Appendix.

The influence of the honeycomb end-wall relative to a smooth casing was examined by numerical simulation. A comparison of the over-tip leakage mass flow rate and the cavity windage between the smooth and honeycomb end-walls is shown in Fig.8. The leakage mass flow rate is expressed as a percentage of the annulus mass flow rate and the cavity windage is expressed as a moment coefficient. Relative to the smooth end-wall, there is a lower leakage mass flow rate across the honeycomb case, but with increased cavity windage. The reduced axial flow velocity and mass flow through the seal is associated with the interaction with the honeycomb cells. The reduced tangential flow velocity results in a steeper velocity gradient at the rotor surface and hence increased windage.

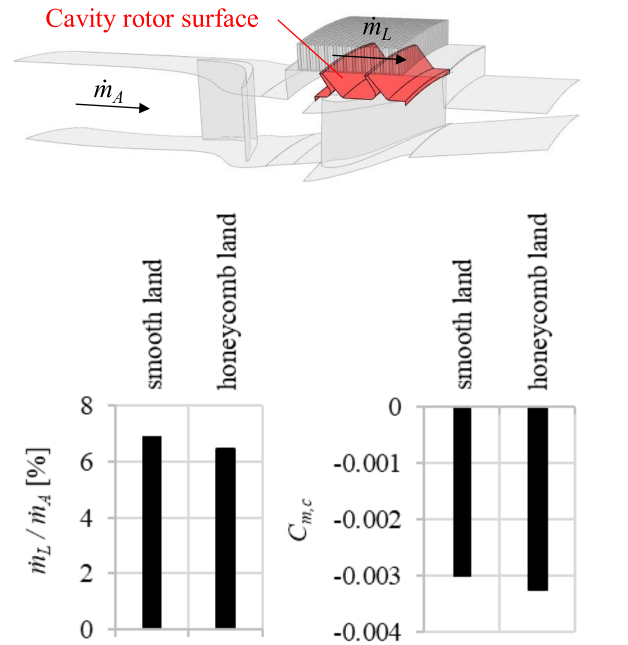

FIGURE 8: NUMERICAL OVER-TIP LEAKAGE AND CAVITY WINDAGE FOR SMOOTH AND HONEYCOMB END-WALLS

The consistent validation with experiment was encouraging and the FCC was subsequently designed and developed through numerical simulation, as discussed in the next Section. The FCC was validated by experiment, with the results presented in Section 5.

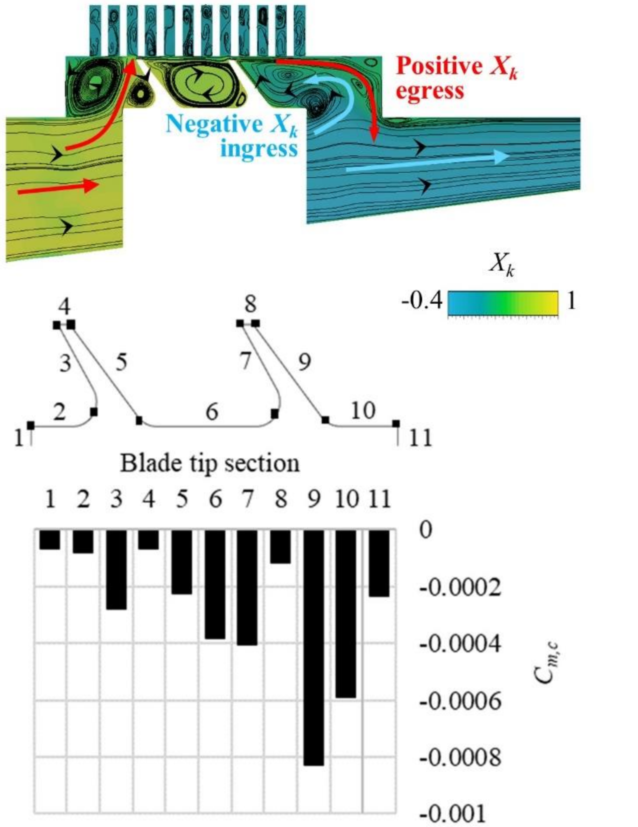

FIGURE 9: FLOW FIELD AND WINDAGE BREAKDOWN IN THE BASELINE SHROUD CAVITY

4. FLOW CONTROL CONCEPT

The flow control objective is twofold: (1) reduce the mixing loss generated where the leakage flow re-enters the main gas path downstream of the blade row, and (2) reduce windage loss from the over-tip cavity. The first step was to identify the flow features contributing to windage and mixing losses using the baseline geometry. A flow control strategy was then designed to mitigate the negative effects.

The schematic arrows on the swirl contour plot in Fig.9 show the cavity ingress and egress flows. The egress from the downstream cavity (marked positive X_k egress) enters the main gas path with a positive swirl-ratio and a strong component of radial velocity as it encounters the cavity wall. In contrast, the main gas path has a negative swirl-ratio and a negligible radial component. The resulting shear gives rise to mixing losses. Therefore, from the mixing loss perspective, the flow control strategy should reduce the radial component and the swirl-ratio of the egress from the downstream cavity.

The bar graph in Fig.9 shows a breakdown of the cavity windage. Each bar represents the moment coefficient on a section (marked 1 to 11) of the blade tip i.e., the rotating surfaces inside the cavity. A negative moment coefficient indicates that the moment is opposing the motion of the rotor. The bars in the graph are numbered to correspond to the numbered sections of the blade tip surface. The main contribution to the cavity windage is from rotor surfaces 9-10, situated in the downstream cavity. This is not surprising as the swirl-ratio of the flow here was shown previously to be relatively low. The schematic arrows on the swirl-ratio contour plot indicate this is due to the negative X_k fluid exiting the blade row and being pumped radially into the downstream cavity. It is this ingress that is responsible for the large windage on sections 9-10. From the perspective of cavity windage, the flow control strategy should modify the flow topology to minimize downstream ingress.

Before a flow control strategy was devised to satisfy the aforementioned requirements, the positioning of the concept inside the cavity was also given due consideration. Restrictions were set by the Clean Sky 2 topic manager (industry partner), related to required rotor-stator clearances due to movement of components during transient operation and assembly stack-up uncertainty. The restricted design space is shown in Fig.10(a). Within these geometric constraints, the FCC shown in Fig.10(b) was devised to implement the flow control strategy shown in Fig.10(c). The concept is essentially a row of turning vanes in a U-shape channel. Windage is reduced by deflecting a portion of the over-tip leakage onto the rotor to create a recirculating region

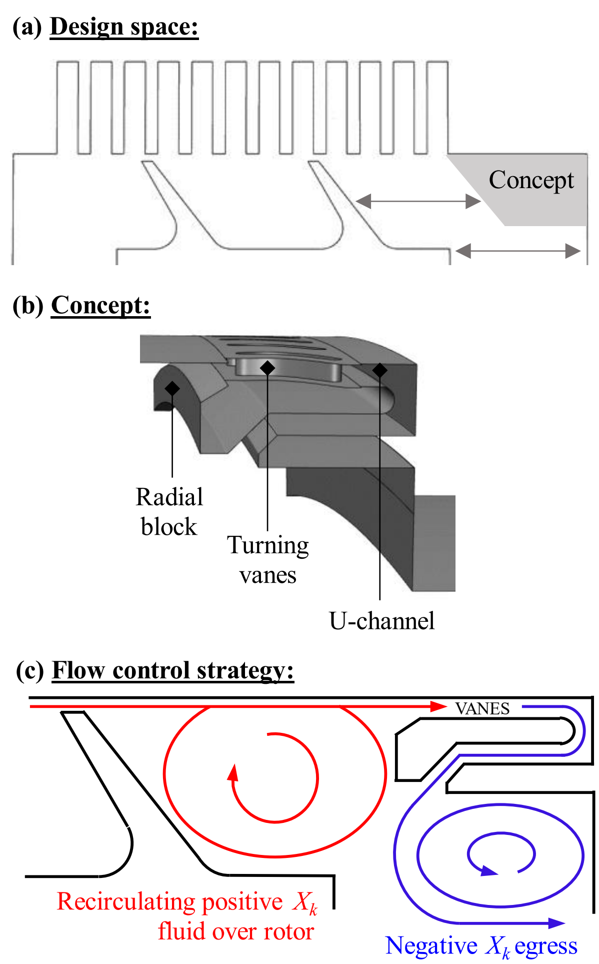

FIGURE 10: FLOW CONTROL CONCEPT – THE DESIGN SPACE, FCC, AND FLOW CONTROL STRATEGY

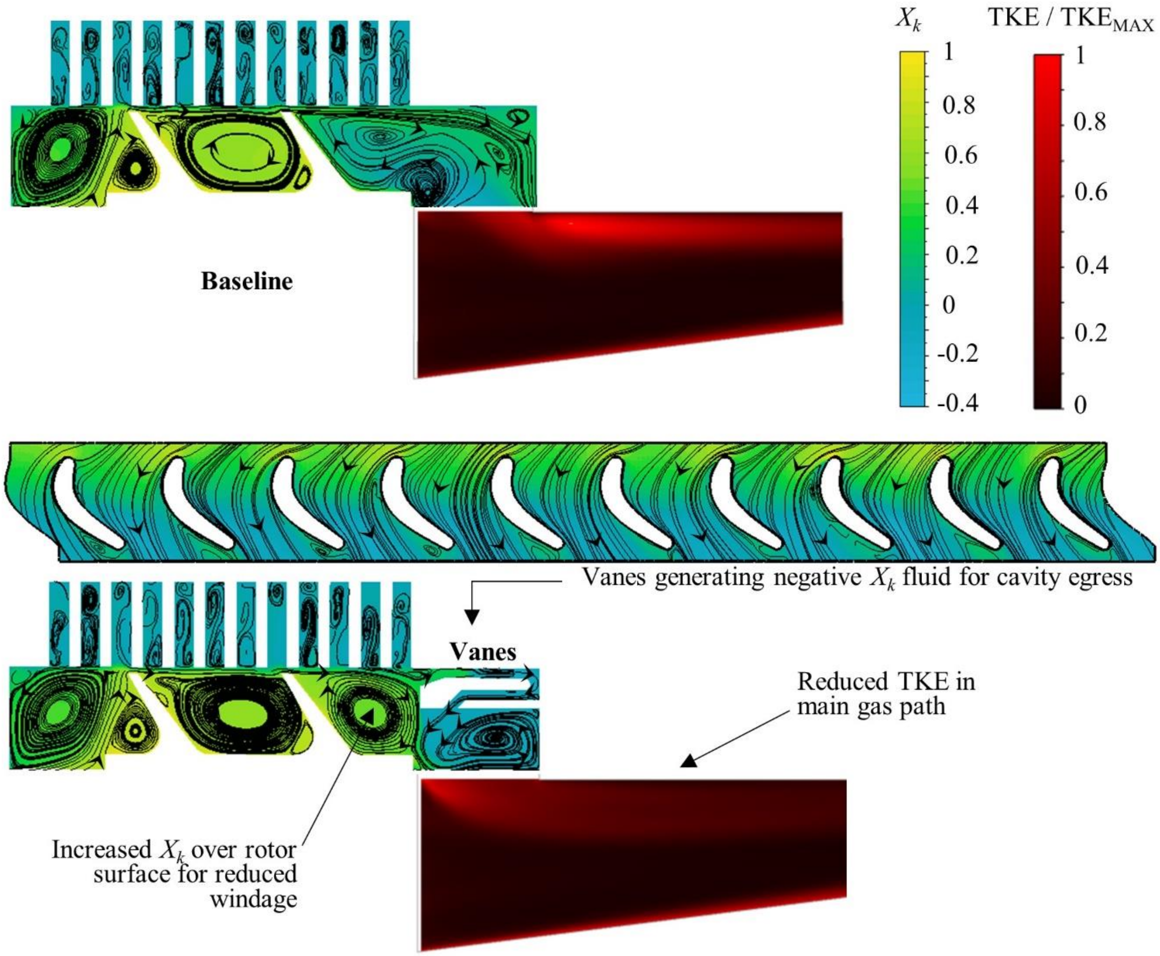

FIGURE 11: CONTOURS OF SWIRL-RATIO AND TURBULENT KINETIC ENERGY FOR BASELINE AND FCC CASES

of positive X_k fluid over the rotor surface. The portion of leakage that is not deflected traverses the U-shape channel with the turning vanes. The vanes turn the flow to better match the egress swirl-ratio of the main gas path and the channel reduces the component of radial velocity. The redirected leakage flow acts to suppress the ingress of mainstream fluid pumped radially into the over-tip cavity by the rotor.

Numerical results from the simulations of the proposed FCC and the baseline are shown in Fig. 11. The over-tip cavity in both cases is shown with contours of time-averaged and circumferentially-averaged swirl-ratio with superimposed in-plane average streamlines. The streamlines show that the FCC modifies the flow topology as intended. A portion of the leakage flow exiting the labyrinth seal is deflected, forming a recirculating region of positive X_k over the rotor surface; another portion of the leakage flow traverses the U-shape channel, where the turning vanes convert the positive swirl-ratio to a negative X_k, similar to that of the main gas path.

The flow through the turning vanes is also illustrated in Fig.11, where the average X_k contours and streamlines are shown at midspan. The leading-edge angle of the turning vanes (+55 degrees) was matched to the velocity angle of the oncoming leakage flow, which was determined from the baseline flow. The trailing-edge angle of the turning vanes (-23 degrees) was matched to the velocity angle in the main gas path. Due to the constrained design space in the axial direction (chord length = 16 mm), the velocity angle could not be matched at the trailing edge without excessive camber, which was a limiting factor in achieving better flow guidance through the vanes. The solidity of the turning vanes was briefly investigated, and the flow was found to be invariable beyond a solidity of unity.

The main gas path (or annulus) downstream of the blade is shown in Fig.11 with contours of the average turbulent kinetic energy (TKE). The TKE has been normalized using its maximum value in the contoured region and is used to visualize the mixing - shear leads to the generation of turbulence, that is to the generation of turbulence kinetic energy. Relative to the baseline, there is less TKE generated with the FCC and hence reduced mixing loss.

The change of the moment coefficient on the blade tip sections with the FCC included in the cavity is shown in Fig.12(a). The moment coefficient for sections 9-11 becomes

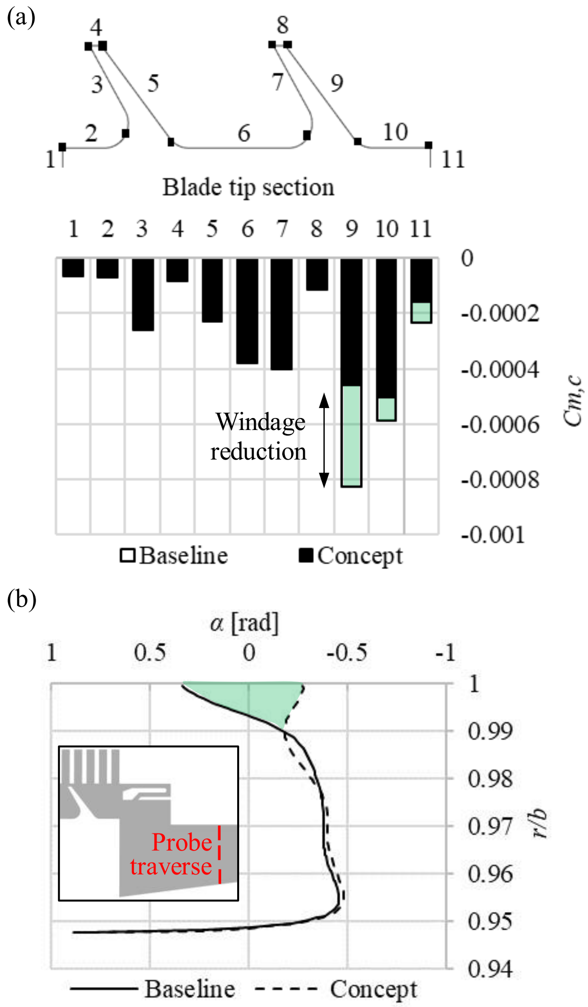

FIGURE 12: COMPARISON OF THE CAVITY WINDAGE BREAKDOWN AND VELOCITY ANGLE DOWNSTREAM OF THE CAVITY BETWEEN BASELINE AND FCC

less negative when the FCC is included, with reduced windage on the intended rotor surfaces. The cumulative reduction in cavity windage is 16% relative to the baseline.

The velocity angle in the main gas path downstream of the over-tip cavity for the baseline and FCC is shown in Fig.12(b). The velocity angle is both time- and circumferentially-averaged. The velocity angle in the near shroud region is better aligned with that of the main gas path when the FCC is included, with a more uniform distribution across the annulus. This improved uniformity of velocity angle is consistent with the reduction in generated TKE.

The channel inlet height of the FCC (*h* in Fig.13) was optimized through a parametric study. The height controls the proportion of fluid deflection relative to the amount passing through the U-shape channel and influences the FCC performance. The optimization was limited to the FCC inlet due to the constrained design space in the radial direction and the practical minimum-thickness requirements for additive manufacture. The optimization process monitored the mass flow rate through the FCC, the change in moment coefficient on the blade tip relative to the baseline (i.e., the cavity windage reduction), and the change of TKE in the main gas path downstream of the cavity outlet relative to the baseline (i.e., the TKE reduction). The TKE was integrated over a circumferential cross-section of the periodic sector. The trends of these parameters as a function of the FCC channel inlet dimension (*h/s*) are shown in Fig.13; here the inlet height, *h*, on the abscissa is non-dimensionalized with respect to the minimum radial clearance in the labyrinth seal, *s*. Simulations were performed for the inlet heights *h/s = 0, h/s* = 1.6, *h/s* = 3.8, and *h/s* = 5.2. Note that *h/s = 0* represents a fully blocked channel.

In Fig.13(a), the mass flow rate through the FCC is non-dimensionalized with respect to the mass flow rate of the total leakage flow. The mass flow rate through the FCC is seen to increase as the inlet height increases, as would intuitively be expected. The mass flow becomes invariable for *h/s > 3*. The variation of cavity windage reduction, $\Delta C_{m,\,c}$, and TKE reduction with *h/s* are shown in Fig.13(b). Note that the windage

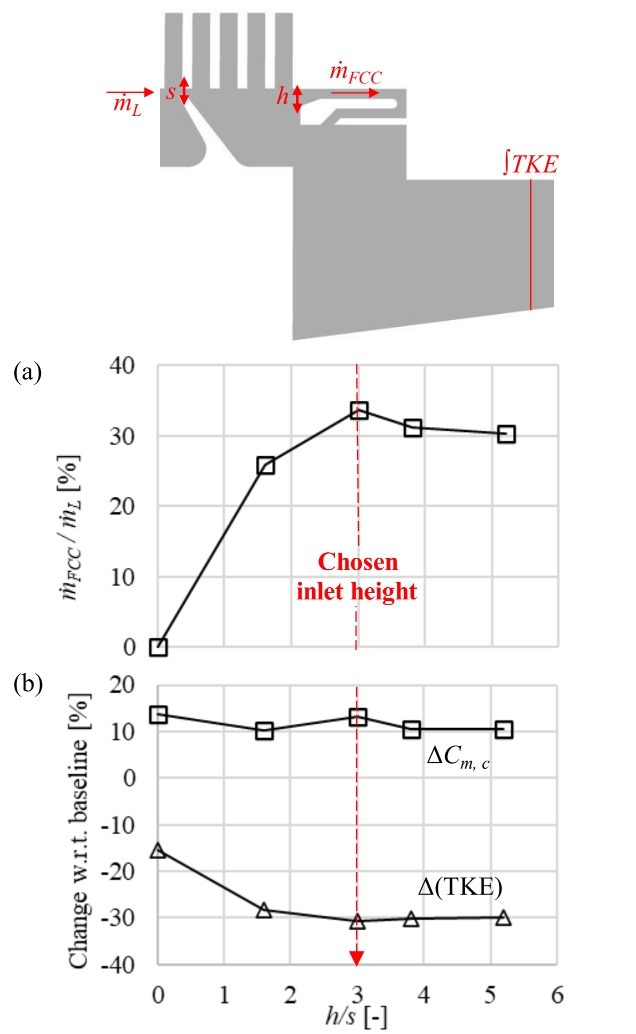

FIGURE 13: OPTIMIZATION OF FCC — PERFORMANCE WITH RESPECT TO INLET HEIGHT

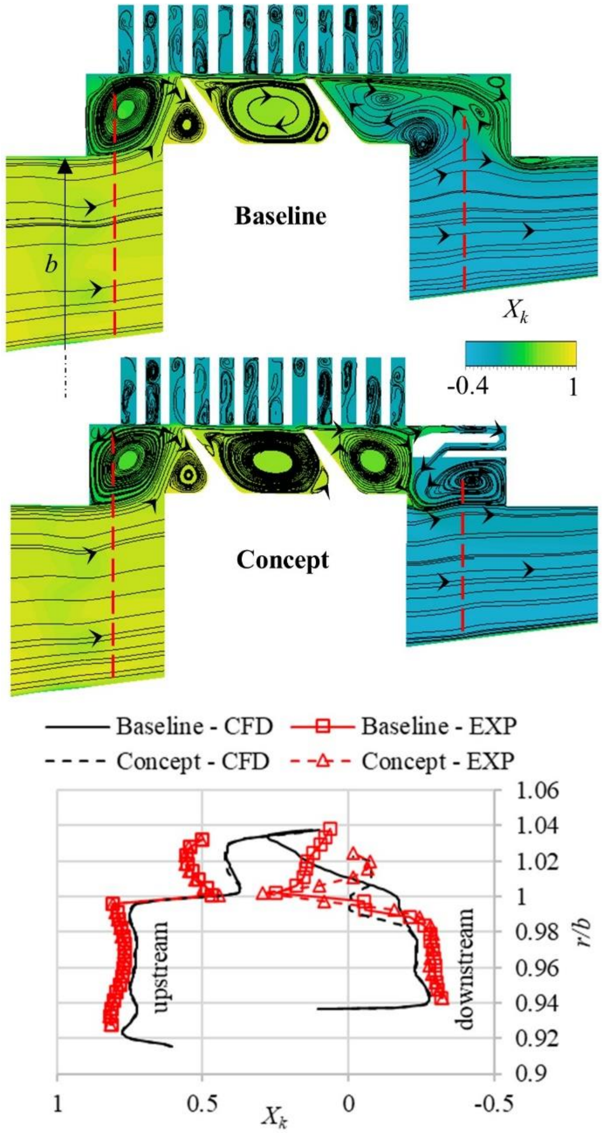

FIGURE 14: COMPARISON OF NUMERICAL AND EXPERIMENTAL SWIRL-RATIO DISTRIBUTIONS BETWEEN BASELINE CAVITY AND CAVITY WITH CONCEPT

torque is negative when it is against the direction of rotation and therefore a positive $\Delta C_{m,c}$ indicates a reduction in cavity windage torque. It is instructive to observe these variations in conjunction with the variation in mass flow rate. The cavity windage reduction remains stable as the mass flow rate through the concept increases. This indicates that although the amount of fluid recirculating over the rotor is decreasing as *h/s* increases, there is no significant ingestion of negative X_k fluid. Hence, this suppression of ingestion remains effective even when there is a minimum amount of leakage flow being recirculated. In contrast, the beneficial reduction in TKE increases with increasing mass flow rate through the FCC because the amount of egress fluid (with negative X_k) being supplied to the annulus is increasing. It is helpful to reiterate that the FCC splits the leakage flow into two portions: part of the flow passes through the FCC and is converted to the swirl-ratio of the main gas path, while the swirl-ratio of the recirculated portion is not converted. Ultimately, the total leakage flow rate will exit the cavity. Hence, the greater the proportion that traverses the FCC to better match the X_k of the main gas path, the more favorable will be the outcome in terms of annulus TKE reduction.

The parametric study shows that an inlet height *h/s* = 3 is sufficient to achieve an optimum FCC performance – there is no benefit beyond this point, and this was the chosen inlet height.

The FCC, after being developed and optimized through numerical simulation, was then created physically using an additive manufacturing process and installed in the experimental rig for testing and validation.

5. VALIDATION

The numerical prediction for the performance of the FCC was validated against experimental measurement: first, the distribution of swirl-ratio upstream and downstream of the blade; and second, the change in rotor windage torque between baseline and FCC. The former comparison assesses whether the resulting flow topology forms as intended, and the latter comparison assesses the accuracy of the combined reduction of the windage and mixing losses. It is important to recognize that the influence of the FCC on mixing loss generates a change in the windage for the rotor blade: a change in the velocity angle downstream of the blade results in a change of the flow at the shroud of the blade. Thus, the rotor windage torque provides a measure of the combined reduction of cavity windage and mixing losses.

The radial variation of swirl-ratio upstream and downstream of the blade for both the baseline and FCC configurations are shown in Fig.14. These distributions of X_k were taken along the dashed datum lines superimposed on the contour maps. Here, X_k is both time- and circumferentially-averaged. The in-plane average streamlines have also been superimposed. The blade shroud is located at r/b = 1. The numerical and experimental distributions of X_k are qualitatively similar, with some quantitative discrepancies inside the over-tip cavity (r/b > 1). While the upstream swirl-ratio distribution is identical for the baseline and FCC cases, there are significant differences in the downstream distribution inside the cavity and in the near cavity region of the annulus. Hence, the FCC has

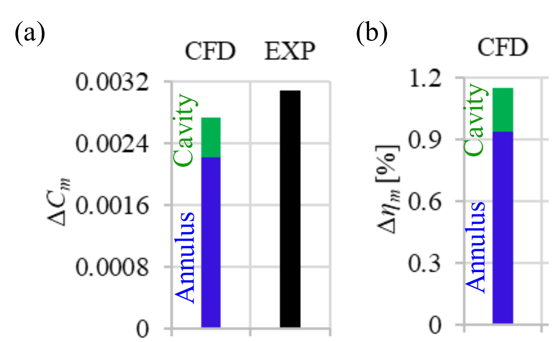

FIGURE 15: CHANGE IN MOMENT COEFFICIENT AND MECHANICAL EFFICIENCY BETWEEN BASELINE AND FCC

influenced the swirl-ratio distribution in the intended region, as expected. The main region of influence is 1.02 > r/b > 0.98, where X_k for the FCC changes relative to the baseline. The contour plots (with the in-plane streamlines) show this region is influenced by egress from the cavity. In the baseline flow, the cavity egress occurred further downstream near the cavity end-wall, but the change in topology with the FCC has moved the egress upstream. This feature is also captured experimentally - despite some quantitative discrepancy, there is good qualitative consistency with the simulation.

The comparison between the numerically predicted and the experimentally measured change in rotor windage due to the FCC is shown in Fig.15(a). The change is expressed in terms of a moment coefficient. The numerical result has been decomposed into the fraction from the rotor surface inside the cavity (i.e., due to the blade tip), and the fraction from the rotor surface inside the annulus (i.e., the blade). The predicted change in rotor windage is in good agreement with the experiment —the numerical prediction is consistent within 10% of the experimental measurement. The breakdown of the numerical result shows that the main contribution to the change in moment coefficient is from the annulus. This is due to the improved flow around the blade as a result of the FCC producing a velocity angle near the blade shroud that is better aligned with the blade's flow exit angle.

The change in mechanical efficiency due to the change in rotor windage torque is shown in Fig.15(b). Mechanical efficiency is calculated using Eq.4 [18], which is the ratio of the output mechanical energy to the isentropic change in enthalpy across the turbine stage. In Eq.4, η_m is mechanical efficiency, M is the rotor moment torque, Ω is the rotor angular velocity, $\dot{m}_A$ is the annulus mass flow rate, C_p is the specific heat capacity of air at constant pressure, T_{in} is the total temperature at the stage inlet, P_{in} is the total pressure at the stage inlet, and P_{out} is the total pressure at the stage outlet. The FCC increases the mechanical efficiency of the turbine stage by 1%. Note that this calculation is for the stage in isolation and does not account for the influence of the changes of the flow on the downstream stages.

$$\Delta\eta_m = \frac{\Delta M \cdot \Omega}{\dot{m}_A C_p T_{in}\left[1 - \left(\frac{P_{out}}{P_{in}}\right)^{\frac{\gamma-1}{\gamma}}\right]} \qquad (4)$$

6. PRACTICAL IMPLICATIONS

The key contributions and innovations of this study are summarized here. This research was a response to the EU Clean Sky 2 programme, exploring the use of additive manufacturing (AM) for flow control devices to reduce windage torque in LPT over-tip leakage cavities. Numerical simulation was used to create a flow-control concept, which was subsequently manufactured using AM and tested in an engine-representative test rig at low TRL. From a practical perspective, scaling to the engine would only be strictly appropriate for the geometry used in the experiments and subject to the limits of dimensional similitude. We would expect engine designers to validate their CFD codes on the experimental rig conditions and extrapolate to higher Mach numbers and Reynolds numbers. However, the proof-of-concept would be valid and can be implemented into the engine design process. The research has extended the design envelope for AM technology and provided a potential prototype appropriate for an engine demonstrator at higher TRL.

7. CONCLUSION

A joint numerical and experimental campaign has introduced an optimized flow control concept (FCC) to reduce both the windage torque and the mixing losses in an LPT over-tip cavity. The FCC was a device incorporating a row of turning vanes in the downstream chamber of the cavity; the device redirected positively swirling flow onto the downstream face of the rotor fin to reduce the windage, while the incorporated vanes turned the over-tip leakage in the direction of the main annulus flow to minimize mixing losses. The concept was optimized to perform effectively with an engine-representative honeycomb end-wall at cruise flight conditions.

The experiments were conducted in a cold-flow axial turbine rig, which simulated the flow paths in an LPT over-tip cavity at fluid-dynamically scaled conditions. An in-line torque meter was used to measure the change in windage between the baseline honeycomb end-wall and the FCC. Radial distributions of swirl-ratio were measured using a five-hole probe at two axial positions upstream and downstream of the over-tip cavity and annulus. The numerical and experimental distributions of swirl-ratio were qualitatively consistent, showing the FCC operated as designed.

There was less computed turbulent kinetic energy generated with the FCC (relative to the baseline) and consequently reduced mixing loss, providing further confidence in the flow control strategy. Experiments and computations were consistent with a cumulative reduction in cavity windage of 16%. The FCC is estimated to increase the mechanical efficiency of the turbine stage in isolation by 1%. It is expected the FCC will be tested at higher TRL in an engine demonstrator.

ACKNOWLEDGEMENTS

This project was funded by Clean Sky 2 Joint Undertaking under the European Union's Horizon 2020 research and innovation program (H2020-GAP-886112-ACUHRA). The authors thank Matt Hawthorne at Added Scientific Ltd for his support in this project. The calculations were performed using the University of Nottingham HPC Facility and Sulis at HPC Midlands Plus, which was funded by EPSRC grant EP/T022108/1.

NOMENCLATURE

LPT	Low-pressure turbine
FCC	Flow control concept
b	Shroud radius
U	Rotor speed
N	Rotor speed in revolutions per minute
rpm	Revolutions per minute
M	Torque

Ω	Rotor angular velocity
V_t	Tangential flow velocity
X_k	Swirl-ratio
$X_{k,\,in}$	Swirl-ratio of cavity ingress
PR	Pressure ratio
p	Static pressure
p_1	Static pressure upstream of cavity
z	Axial coordinate
L	Cavity length
$\dot{m}_A$	Annulus mass flow rate
$\dot{m}_L$	Leakage mass flow rate
$\dot{m}_{FCC}$	Through-concept mass flow rate
$C_{m,\,c}$	Cavity moment coefficient
C_m	Rotor moment coefficient
Re_Φ	Reynolds number
α	Velocity angle
s	Seal clearance
h	Concept inlet height
TKE	Turbulent kinetic energy
C_P	Air heat capacity at constant pressure
γ	Air heat capacity ratio
P_{in}	Total pressure at inlet of turbine stage
P_{out}	Total pressure at outlet of turbine stage
T_{in}	Total temperature at inlet of turbine stage
η_m	Mechanical efficiency of turbine stage

REFERENCES

[1] Li, Z., Christodoulou, L., Jefferson-Loveday, R. J., Ambrose, S., Jackson, R., Lock, G. D., Sangan, C. M., and Scobie, J. "Windage Torque Reduction in Low-Pressure Turbine Cavities Part 1: Concept Design and Numerical Investigations." ASME. *J. Turbomach*. doi: https://doi.org/10.1115/1.4064224.

[2] Jackson, R., Li, Z., Christodoulou, L., Ambrose, S., Sangan, C., Jefferson-Loveday, R. J., Lock, G. D., and Scobie, J. "Windage Torque Reduction in Low-Pressure Turbine Cavities Part 2: Experimental and Numerical Results." ASME. *J. Turbomach*. doi: https://doi.org/10.1115/1.4063876.

[3] Jackson, R., Christodoulou, L., Li, Z., Sangan, C. M., Ambrose, S., Jefferson-Loveday, R. J., Lock, G. D., and Scobie, J. Influence of swirl and ingress on windage losses in a low-pressure turbine stator-well cavity. *Exp Fluids* 64, 173 (2023). https://doi.org/10.1007/s00348-023-03715-7.

[4] Pfau, A., Treiber , M., Sell, M., and Gyarmathy, G. (February 1, 2000). "Flow Interaction From the Exit Cavity of an Axial Turbine Blade Row Labyrinth Seal." ASME. *J. Turbomach.* April 2001; 123(2): 342–352. https://doi.org/10.1115/1.1368124

[5] Pfau, A., Schlienger, J., Rusch, D., Kalfas, A. I., and Abhari, R. S., 2003, "Unsteady Flow Interactions Within the Inlet Cavity of a Turbine Rotor Tip Labyrinth Seal," ASME Turbo Expo 2003, Collocated With the 2003 International Joint Power Generation Conference, American Society of Mechanical Engineers, pp. 187–199.

[6] Perini, M., Binder, N., Bousquet, Y., and Schwartz, E. (October 4, 2023). "Rotating Instabilities in Shrouded Low Pressure Turbine at Design and Off-Design Conditions." ASME. *J. Turbomach.* November 2023; 145(11): 111006. https://doi.org/10.1115/1.4063247.

[7] Denton, J. D., 1993, "Loss Mechanisms in Turbomachines," ASME *J. Turbomach*., 115(4), pp. 621–656.

[8] Palmer, T. R., Tan, C. S., Zuniga, H., Little, D., Montgomery, M., and Malandra, A., 2016, "Quantifying Loss Mechanisms in Turbine Tip Shroud Cavity Flows," ASME *J. Turbomach*., 138(9), p. 091006.

[9] Anker, JE, & Mayer, JF. "Simulation of the Interaction of Labyrinth Seal Leakage Flow and Main Flow in an Axial Turbine." Proceedings of the ASME Turbo Expo 2002: Power for Land, Sea, and Air. Volume 5: Turbo Expo 2002, Parts A and B. Amsterdam, The Netherlands. June 3–6, 2002. pp. 217-224. ASME. https://doi.org/10.1115/GT2002-30348.

[10] Bohn, D, Krewinkel, R, Tu¨mmers, C, & Sell, M. "Influence of the Radial and Axial Gap of the Shroud Cavities on the Flowfield in a 2-Stage Turbine." Proceedings of the ASME Turbo Expo 2006: Power for Land, Sea, and Air. Volume 6: Turbomachinery, Parts A and B. Barcelona, Spain. May 8–11, 2006. pp. 821-830. ASME. https://doi.org/10.1115/GT2006-90857.

[11] Jia, W., Liu, H. Numerical Investigation of the Interaction between Mainstream and Tip Shroud Leakage Flow in a 2-Stage Low Pressure Turbine. *J. Therm. Sci*. 23, 215–222 (2014). https://doi.org/10.1007/s11630-014-0698-2.

[12] Pfau, A., Kalfas, A. I., and Abhari, R. S. (March 1, 2004). "Making Use of Labyrinth Interaction Flow." ASME. *J. Turbomach.* January 2007; 129(1): 164–174. https://doi.org/10.1115/1.2218571.

[13] Rosic, B. and Denton, J.D., 2008, "Control of Shroud Leakage Loss by Reducing Circumferential Mixing," ASME. *J. Turbomach.,* 130(2), p. 021010.

[14] Rosic, B., Denton, J.D., Curtis, E.M. and Peterson, A.T., 2008, "The Influence of Shroud and Cavity Geometry on Turbine Performance: An Experimental and Computational Study— Part II: Exit Cavity Geometry. ASME. *J. Turbomach*., 130(4), p. 041002.

[15] Wallis, A.M., Denton, J.D. and Demargne, A.A.J., 2000, "The Control of Shroud Leakage Flows to Reduce Aerodynamic Losses in a Low Aspect Ratio, Shrouded Axial Flow Turbine," ASME. *J. Turbomach*., 123(2), pp. 334-341.

[16] Gao, J., Zheng, Q., Yue, G. and Sun, L., 2012, "Control of Shroud Leakage Flows to Reduce Mixing Losses in a Shrouded Axial Turbine," Proceedings of the Institution of Mechanical Engineers, Part C: *Journal of Mechanical Engineering Science*, 226(5), pp. 1263-1277.

[17] Ghaffari, P, Willinger, R, Bauinger, S, & Marn, A. "Impact of Passive Tip-Injection on Tip-Leakage Flow in Axial Low Pressure Turbine Stage." Proceedings of the ASME Turbo Expo 2015: Turbine Technical Conference and Exposition. Volume 2A: Turbomachinery. Montreal, Quebec, Canada. June 15–19, 2015. V02AT38A002. ASME. https://doi.org/10.1115/GT2015-42226.

[18] Hudson, T., and Coleman, W., 2000. "Analytical and experimental assessment of two methods of determining turbine

efficiency." *Journal of Propulsion and Power*, 16(5), pp.760-767.

[19] Vectoflow Probe Manual, Vectoflow Gmbh (2017). URL: https://vectoflow.de/wp-content/uploads/2023/09/2023-09-15_Standard-multihole-probe_Datasheet_EN.pdf

[20] Ruchala, P., Grabowska, K., Malachowski, P, Santos, L., and Back, D, 2018, Use and Calibration of 5-Hole Pressure Probes to Measurement of Airflow Velocity, *Journal of KONES Powertrain and Transport*, 25(2).

APPENDIX

The uncertainty in the pressure measurements across the over-tip in Figure 7 is shown in Figure 16 below. The transducers had a range of 0-400 mbar and an accuracy of ± 0.3% of the full-scale range (± 1.2 mbar).

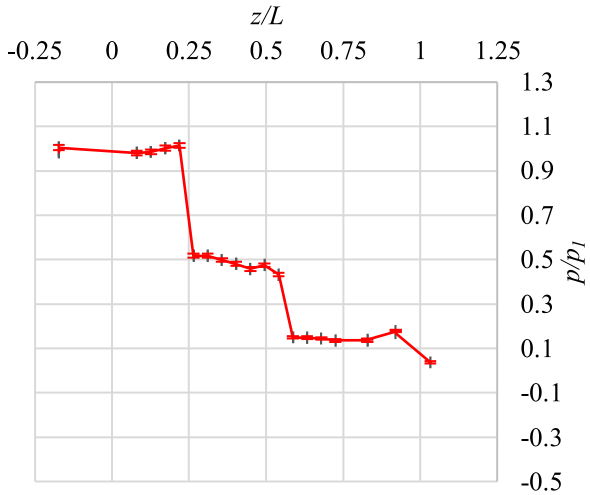

FIGURE 16: EXPERIMENTAL PRESSURE MEASUREMENTS ON THE SMOOTH END-WALL SHOWING MEASUREMENT UNCERTAINTY FOR DATA IN FIGURE 7

The local velocity components and corresponding angles of the flow upstream and downstream of the tip cavity were determined using pressure measurements from a custom five-hole probe (manufactured by Vectoflow GmbH). Flow angles and velocities were derived by applying the data to calibration coefficients provided by Vectoflow [19], following their in-house calibration of the probe. Flow angles are accurate to < ± 1°, though Ruchala et al. [20] state the accuracy to be < ± 0.2°. The uncertainty in velocity depends on the range of the pressure scanner, which in this case was 345 mb. Figure 17 shows the uncertainty on the swirl measurements for all the tested configurations.

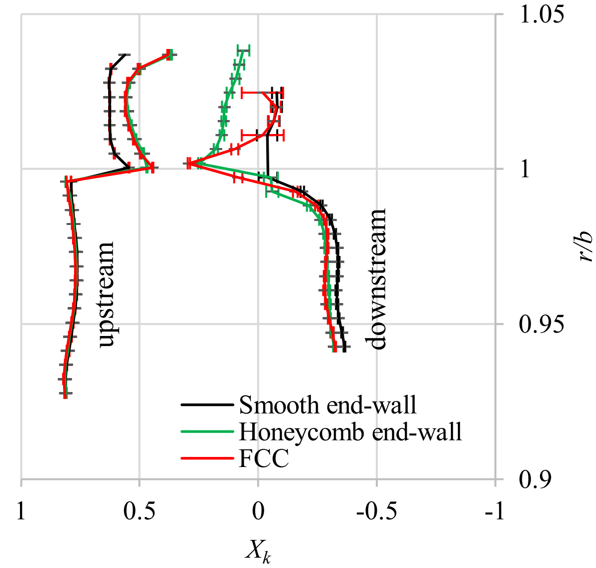

FIGURE 17: UPSTREAM AND DOWNSTREAM EXPERIMENTAL VARIATION OF X_k WITH RADIUS SHOWING MEASUREMENT UNCERTAINTY FOR DATA PRESENTED IN FIGURES 7 AND 14

LIST OF TABLES

LIST OF FIGURES